



Contents lists available at ScienceDirect

Journal of Sound and Vibration

journal homepage: www.elsevier.com/locate/jsvi

Comparing the floquet stability of open and breathing fatigue cracks in an overhung rotordynamic system



Philip Varney*, Itzhak Green

Georgia Institute of Technology, Woodruff School of Mechanical Engineering, 801 Ferst Drive, Atlanta, GA 30332, United States

ARTICLE INFO

Article history:

Received 28 November 2016

Received in revised form

29 May 2017

Accepted 19 July 2017

Handling Editor: W. Lacarbonara

Available online 27 July 2017

Keywords:

Rotordynamics

Stability

Rotor cracks

Floquet theory

Diagnostics

ABSTRACT

Rotor cracks represent an uncommon but serious threat to rotating machines and must be detected early to avoid catastrophic machine failure. An important aspect of analyzing rotor cracks is understanding their influence on the rotor stability. It is well-known that the extent of rotor instability versus shaft speed is exacerbated by deeper cracks. Consequently, crack propagation can eventually result in an unstable response even if the shaft speed remains constant. Most previous investigations of crack-induced rotor instability concern simple Jeffcott rotors. This work advances the state-of-the-art by (a) providing a novel inertial-frame model of an overhung rotor, and (b) assessing the stability of the cracked overhung rotor using Floquet stability analysis. The rotor Floquet stability analysis is performed for both an open crack and a breathing crack, and conclusions are drawn regarding the importance of appropriately selecting the crack model. The rotor stability is analyzed versus crack depth, external viscous damping ratio, and rotor inertia. In general, this work concludes that the onset of instability occurs at lower shaft speeds for thick rotors, lower viscous damping ratios, and deeper cracks. In addition, when comparing commensurate cracks, the breathing crack is shown to induce more regions of instability than the open crack, though the open crack generally predicts an unstable response for shallower cracks than the breathing crack. Keywords: rotordynamics, stability, rotor cracks.

© 2017 Elsevier Ltd. All rights reserved.

1. Introduction

Rotor cracks, though rare, are exceptionally dangerous and can result in catastrophic machine failure [1,2]. Thus, rotor cracks represent an uncommon but serious threat to rotating machines and must be detected early to avoid catastrophic failure. A necessary prerequisite for understanding the behavior of a cracked rotor is a thorough study of the associated rotordynamics, including both a forced response analysis (i.e., the diagnostic signatures of the crack) and a stability analysis. It is well-known that deeper cracks result in rotor instability at lower shaft speeds [3]. Consequently, propagating rotor cracks can eventually result in catastrophic instability even if the operational shaft speed remains constant.

The first step in determining the stability of a cracked rotor is accurately modeling the crack. In general, rotor cracks are modeled according to (a) how the crack faces behave and (b) how the crack compliance is calculated. The faces of an open crack remain open regardless of shaft rotation or loading conditions [4–6], while those of a breathing crack open and close

* Corresponding author.

E-mail addresses: pvarney3@gatech.edu (P. Varney), itzhak.green@me.gatech.edu (I. Green).

as the crack cross-section varies between tension and compression [7,8]. This difference prominently manifests when modeling the additional rotor compliance contributed by the crack. The open crack results in a rotor stiffness which is constant in a shaft-fixed reference frame, whereas a breathing crack results in a nonlinear or linear time-periodic stiffness matrix even in the shaft-fixed frame. In either case, the inertial stiffness of the rotor is linear time-periodic, and possibly nonlinear depending of the specific breathing model used to approximate the crack.

Most approaches for modeling crack breathing behavior are either orientation-dependent [9–11] or response-dependent [12,13]. Orientation-dependent models assume that the crack geometry varies smoothly between the fully-opened and fully-closed states, and thus, the crack compliance only depends on the shaft rotation angle. These models are generally valid beneath the first rotor critical speed [9]. The advantage of modeling an orientation-dependent crack is that the compliance is a known function of shaft rotation, and can be determined prior to simulating the rotordynamics. On the other hand, modeling the crack breathing as response-dependent assumes that the extent of crack closure depends on the rotordynamics, and therefore must be evaluated at each instant in the numeric simulation (and consequently, the response can be nonlinear). Darpe et al. [13] develop the crack-closure line approach, where the boundary between the opened and closed crack regions is determined by the instantaneous stress state at the crack. Other works assume that the crack is always either fully-opened or fully-closed [14]; this type of switching crack is not considered here because it predicts responses which are not observed in reality [15].

Rotor cracks manifest most fundamentally as an increase in rotor compliance (i.e., a reduction in rotor stiffness). The total compliance is therefore found by summing the undamaged rotor compliance and the additional compliance introduced by the crack. The most common method for calculating the compliance of a true fatigue crack is the strain energy release rate (SERR). The SERR was first developed by Dimarogonas et al. [4], and subsequently expanded to six coupled rotor degrees-of-freedom [16,17]. A thorough survey of the SERR method is presented by Papadopoulos [7], who summarizes works employing the method, modifications to the method, and avenues for future work. Other researchers approximate the crack compliance using local area moments of inertia [5,18] or three-dimensional finite element analysis [19,20].

Many crack detection schemes rely on integer shaft speed harmonics to identify rotor cracks. In the presence of a constant radial load (e.g., gravity), an open crack generates only a 2X harmonic [5], whereas a breathing crack induces many integer harmonics of the shaft speed [2,7]. Importantly, these harmonic oscillations interact with the structure and cause associated sub-synchronous critical speeds (e.g., the 1/2 critical speed). The loss of rotor stiffness with increasing crack depth causes these sub-synchronous critical speeds to likewise decrease. Other important diagnostic signatures are also used to characterize rotor cracks, such as coupling phenomena [16] and unique time-energy-frequency signatures [21–23,10].

A powerful technique for determining the stability of linear time-periodic dynamic systems is Floquet stability analysis [24,25]. Guilhen et al. [26] describe a numeric method for performing Floquet stability analysis, and use the method to calculate the instability threshold speed of an asymmetric rotor. Huang et al. [27] likewise perform a Floquet stability analysis of a simple rotor model where the crack compliance is obtained using the SERR; their results indicate that even a small amount of damping can dramatically improve the rotor instability threshold (this conclusion is likewise corroborated by other investigations [28,29]). A similar analysis is performed by Meng and Gasch [30], who consider the stability of a flexible Jeffcott rotor supported by fluid film bearings. Interestingly, their work concludes that the type of bearing does not generally influence the shaft speeds over which the rotor response is unstable. Another important conclusion from existing stability analyses of cracked rotors is that the breadth and onset of rotor instability is strongly dependent on the crack depth and location [31,29]; deeper cracks result in wider instability regions and an earlier onset of unstable response. Sinou [32] reaches similar conclusions using a perturbation stability analysis. Luo et al. [33] use Floquet stability analysis to indicate that the multiple-fault scenario with a crack and rotor-stator rub changes the stability characteristics of the system. Ricci and Pennacchi [34] analyze the stability of a generator rotor and conclude that in their particular system, instability is eliminated because the crack is a localized effect in comparison to the large overall system geometry.

The objective of this work is to expand a model of an overhung rotor [3,5] and use the improved model to compare the rotor stability considering both an open crack and a breathing crack. The inertial-frame overhung rotor model consists of four degrees-of-freedom, including lateral and angular rotor deflections. External viscous damping and internal structural damping are included in the model, along with rotating imbalance and dynamic angular misalignment. The crack compliance is found using the strain energy release rate, and crack breathing is instituted using an expedient frequency-domain approximation of the crack compliances over one revolution as calculated using the crack closure line method. Rotor stability is determined using a numeric Floquet stability analysis, and the results are compared for both an open and breathing crack. The specific parameters studied here are the crack depth, the external viscous damping ratio, and the rotor inertia.

2. Modeling the overhung rotor

The four degree-of-freedom rotor model including lateral and angular deflections is shown schematically in Fig. 1 relative to the inertial frame $\xi\eta\zeta$. The rotor has mass m_R and transverse and polar mass moments of inertia of I_{tR} and I_{pR} , respectively. The rotor rotates about the system-fixed ζ axis with rotation rate ω_r . Lateral and angular deflections in the direction of axis i are denoted e_{Ri} and γ_{Ri} , respectively. Torsional and axial rotor degrees-of-freedom are not considered here. The inertial frame rotor equations of motion are developed from the rotating frame equations of motion given by Varney and Green [6]:

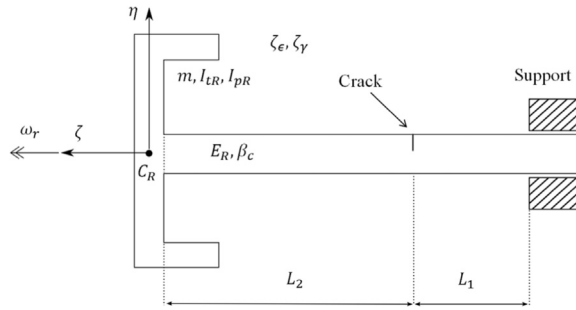


Fig. 1. Schematic of the overhung rotor displaying a transverse fatigue crack.

$$\begin{aligned}
 & \begin{bmatrix} m_R & 0 & 0 & 0 \\ 0 & m_R & 0 & 0 \\ 0 & 0 & I_{tR} & 0 \\ 0 & 0 & 0 & I_{tR} \end{bmatrix} \begin{Bmatrix} \ddot{\epsilon}_{R\xi} \\ \ddot{\epsilon}_{R\eta} \\ \ddot{\gamma}_{R\xi} \\ \ddot{\gamma}_{R\eta} \end{Bmatrix} + \left(\mathbf{D}_R + \mathbf{D}_v + \begin{bmatrix} 0 & 0 & 0 & 0 \\ 0 & 0 & 0 & 0 \\ 0 & 0 & 0 & I_{pR}\omega_r \\ 0 & -I_{pR}\omega_r & 0 & 0 \end{bmatrix} \right) \begin{Bmatrix} \dot{\epsilon}_{R\xi} \\ \dot{\epsilon}_{R\eta} \\ \dot{\gamma}_{R\xi} \\ \dot{\gamma}_{R\eta} \end{Bmatrix} \\
 & + (\mathbf{D}_R^* + \mathbf{K}(t)) \begin{Bmatrix} \epsilon_{R\xi} \\ \epsilon_{R\eta} \\ \gamma_{R\xi} \\ \gamma_{R\eta} \end{Bmatrix} = \begin{Bmatrix} m_R \epsilon_{RG} \omega_r^2 \cos \omega_r t \\ m_R \epsilon_{RG} \omega_r^2 \sin \omega_r t - m_R g \\ (I_{tR} - I_{pR}) \chi_R \omega_r^2 \cos \omega_r t \\ (I_{tR} - I_{pR}) \chi_R \omega_r^2 \sin \omega_r t \end{Bmatrix} \tag{1}
 \end{aligned}$$

where the rotor imbalance is ϵ_{RG} and the dynamic angular misalignment is χ_R [35]. In short-hand form, the equations of motion are:

$$\mathbf{M}_R \ddot{\mathbf{q}}_R + (\mathbf{D}_R + \mathbf{D}_v + \mathbf{G}_R) \dot{\mathbf{q}}_R + (\mathbf{K}(t) + \mathbf{D}_R^*) \mathbf{q}_R = \mathbf{F}_R(t) \tag{2}$$

where the degrees of freedom are encapsulated in the following vector:

$$\mathbf{q}_R = \{ \epsilon_{R\xi} \epsilon_{R\eta} \gamma_{R\xi} \gamma_{R\eta} \}^T \tag{3}$$

The stiffness matrix $\mathbf{K}(t)$ is left as a general function of time to accommodate the time-variant stiffness coefficients resulting from the cracked shaft. If the shaft is undamaged (i.e., isotropic), the stiffness matrix is denoted \mathbf{K}_R , and assumes the following form:

$$\mathbf{K}_R = \frac{E_R I}{L} \begin{bmatrix} \frac{12}{L^2} & 0 & 0 & -\frac{6}{L} \\ 0 & \frac{12}{L^2} & \frac{6}{L} & 0 \\ 0 & \frac{6}{L} & 4 & 0 \\ -\frac{6}{L} & 0 & 0 & 4 \end{bmatrix} \tag{4}$$

where E_R is the elastic modulus, I is the cross-section area moment of inertia, and L is the shaft length. These coefficients can be easily modified to account for other shaft geometries and boundary conditions (e.g., bearing support stiffness), though this work only considers the overhung case.

External viscous damping is included in the rotor model via the matrix \mathbf{D}_v to emulate the operating conditions of real turbomachines [35]. For simplicity, external viscous damping effects are assumed to be decoupled such that \mathbf{D}_v acquires a diagonal form. Taking this into consideration, viscous damping ratios ζ_ϵ and ζ_γ are imposed such that

$$\mathbf{D}_v = 2 \begin{bmatrix} \zeta_\epsilon \sqrt{k_{c\epsilon} m_R} & 0 & 0 & 0 \\ 0 & \zeta_\epsilon \sqrt{k_{c\epsilon} m_R} & 0 & 0 \\ 0 & 0 & \zeta_\gamma \sqrt{k_{t\gamma} I_{tR}} & 0 \\ 0 & 0 & 0 & \zeta_\gamma \sqrt{k_{t\gamma} I_{tR}} \end{bmatrix} \tag{5}$$

where $k_{\epsilon\epsilon}$ and $k_{\gamma\gamma}$ are the diagonal entries of \mathbf{K}_R corresponding to eccentric and angular deflections, respectively. Internal damping caused by material hysteresis is encapsulated in the rotating damping matrix $[D_R]$. Here, the rotating damping matrix is proportional to the undamaged shaft stiffness $[K_R]$ by the equivalent viscous damping coefficient β_c [3,5]:

$$\mathbf{D}_R = \frac{1}{2\omega_r} \beta_c \mathbf{K}_R \tag{6}$$

Because the internal damping forces rotate with the shaft, the inertial frame equations incur an additional contribution by transforming the forces to the inertial frame. The matrix \mathbf{D}_R^* is a consequence of this transformation:

$$\mathbf{D}_R^* = \mathbf{R}^T \mathbf{D}_R \mathbf{R} \tag{7}$$

where the matrix \mathbf{R} moves a vector from the inertial to shaft-fixed frame according to the shaft rotation angle $\alpha(t)$:

$$\mathbf{R} = \begin{bmatrix} \cos \alpha & \sin \alpha & 0 & 0 \\ -\sin \alpha & \cos \alpha & 0 & 0 \\ 0 & 0 & \cos \alpha & \sin \alpha \\ 0 & 0 & -\sin \alpha & \cos \alpha \end{bmatrix} \tag{8}$$

3. Modeling the rotor crack

3.1. Open crack

The overhung rotor displaying a transverse fatigue crack is shown in Fig. 1, where the crack is located a distance L_1 from the support (and thus, the rotor is located a distance L_2 from the crack, where $L = L_1 + L_2$). The depth of the crack is a , and the crack half-width is b (see Fig. 2). Because the crack remains open, the crack compliance and shaft stiffness are constant relative to the shaft-fixed $X_R Y_R Z_R$ reference frame, where Z_R signifies the shaft rotation direction. The crack compliance coefficients c_{ij} are found using the strain energy release rate (SERR) [16], and then arranged into a local matrix [4] that relates the additional deflections caused by the crack to the applied loads:

$$\begin{Bmatrix} \epsilon_{X_R} \\ \epsilon_{Y_R} \\ \gamma_{X_R} \\ \gamma_{Y_R} \end{Bmatrix} = \begin{bmatrix} c_{22} & 0 & 0 & 0 \\ 0 & c_{33} & 0 & 0 \\ 0 & 0 & c_{55} & c_{45} \\ 0 & 0 & c_{45} & c_{44} \end{bmatrix} \begin{Bmatrix} F_{X_R} \\ F_{Y_R} \\ M_{X_R} \\ M_{Y_R} \end{Bmatrix} \tag{9}$$

where F and M are forces and moments relative to the specified direction. The specific details regarding the compliance calculations are omitted here due to the ubiquitousness of the method; further details can be found in the works by Varney and Green [5,6]. The crack compliances are typically accurate for crack depths up to 80% of the shaft diameter [16]. Previous works have calculated the cross-coupling coefficient c_{45} by integrating over half of the crack width (i.e., 0 to b) and doubling

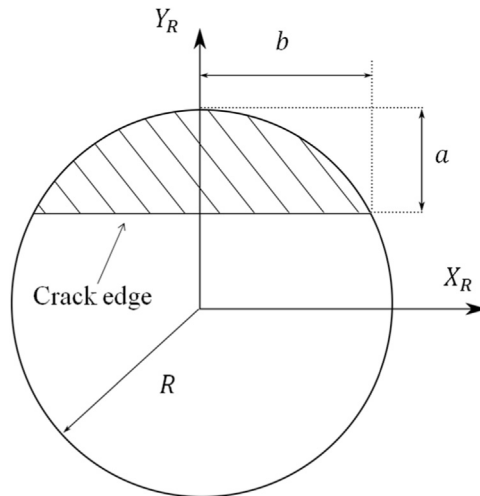


Fig. 2. Crack cross-section relative to the shaft-fixed frame showing the half-width b and depth a .

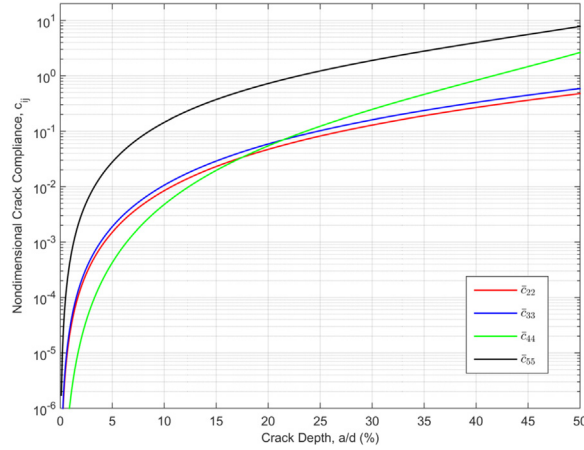


Fig. 3. Non-dimensional compliances for an open fatigue crack ($E_R = 210$ GPa, $\nu = 0.3$, $d = 35$ mm).

the result [3,5]. However, integrating over the full crack width, $-b$ to b , indicates that c_{45} is zero when the crack is fully open. This conclusion is also validated by other researchers [13,7]. The non-dimensional crack compliances are shown in Fig. 3.

The global compliance matrix of the cracked shaft relative to the shaft-fixed frame has previously been obtained using the transfer matrix [36,6]:

$$\mathbf{C}_{rot} = \begin{bmatrix} C_{11} & -c_{45}L_2^2 & c_{45}L_2 & C_{14} \\ -c_{45}L_2^2 & C_{22} & C_{23} & -c_{45}L_2 \\ c_{45}L_2 & C_{32} & C_{33} & c_{45} \\ C_{41} & -c_{45}L_2 & c_{45} & C_{44} \end{bmatrix} \quad (10)$$

where

$$C_{11} = c_{22} + c_{44}L_2^2 + \frac{(L_1 + L_2)^3}{3E_R I} \quad (11)$$

$$C_{22} = c_{33} + c_{55}L_2^2 + \frac{(L_1 + L_2)^3}{3E_R I} \quad (12)$$

$$C_{33} = c_{55} + \frac{(L_1 + L_2)}{E_R I} \quad (13)$$

$$C_{44} = c_{44} + \frac{(L_1 + L_2)}{E_R I} \quad (14)$$

$$C_{14} = C_{41} = c_{44}L_2 + \frac{(L_1 + L_2)^2}{2E_R I} \quad (15)$$

$$C_{23} = C_{32} = -c_{55}L_2 - \frac{(L_1 + L_2)^2}{2E_R I} \quad (16)$$

The final form of the compliance matrix for the open crack is then found by recalling that the coupling compliance coefficient c_{45} is zero for an open crack. Importantly, and necessarily, removing the crack compliances reduces the global compliance matrix to that of an Euler-Bernoulli beam of length $L_1 + L_2$, as expected. The stiffness matrix of the overall cracked shaft is obtained by inverting Eq. (10) and transferring the result into the inertial reference frame:

$$\mathbf{K}(t) = \mathbf{R}^T \mathbf{C}_{rot}^{-1} \mathbf{R} \quad (17)$$

where the matrix \mathbf{R} is provided earlier in Eq. (8). The inertial frame stiffness varies twice per revolution. To understand this conclusion intuitively, consider the cases where the crack is oriented upward (i.e., $Y_R = \eta$) and downward (i.e., $Y_R = -\eta$). Both orientations result in identical cracked shaft stiffness coefficients; thus, the stiffness of any coefficient varies twice per revolution. In the presence of gravity, or any other fixed-direction inertial force, the deflection also varies twice per

revolution because the crack orientation changes with respect to the excitation direction. However, in the case of only synchronous excitation, such as imbalance, the excitation is fixed relative to the crack orientation, and therefore does not create a twice-per-revolution frequency.

3.2. Breathing crack

In reality, the faces of a fatigue crack open and close as portions of the crack alternate between tension and compression. This work assumes that the crack compliances vary harmonically with shaft rotation according to a known function (i.e., the rotor static response dictates the breathing behavior). The crack compliances are found via the crack closure line (CCL) approach [13], where the open region of the crack is determined by the respective stress intensity functions. Then, the compliances are found by integrating only over the open crack region. This approach allows the compliances to reflect the fact that the crack is fully-opened and fully-closed over a finite region of shaft rotation (see Fig. 5), and also permits the cross-coupling compliance c_{45} to be calculated.

The CCL signifies the boundary between the open and closed regions of the crack; the crack compliances are then obtained by integrating across only the open region:

$$c_{22} = \frac{2(1 - \nu^2)}{\pi E_R R} \int_{-b^-}^{b^+} \int_0^a \bar{y} F_{III}^2\left(\frac{y}{h}\right) d\bar{y} d\bar{x} \tag{18}$$

$$c_{33} = \frac{2(1 - \nu^2)}{\pi E_R R} \int_{-b^-}^{b^+} \int_0^a \bar{y} F_{II}^2\left(\frac{y}{h}\right) d\bar{y} d\bar{x} \tag{19}$$

$$c_{44} = \frac{16(1 - \nu^2)}{\pi E_R R^3} \int_{-b^-}^{b^+} \int_0^a \bar{x}^2 \bar{y} F_{IV}^2\left(\frac{y}{h}\right) d\bar{y} d\bar{x} \tag{20}$$

$$c_{45} = \frac{16(1 - \nu^2)}{\pi E_R R^3} \int_{-b^-}^{b^+} \int_0^a \bar{x} \bar{y} \sqrt{1 - \bar{x}^2} F_{IX}\left(\frac{y}{h}\right) F_{IV}\left(\frac{y}{h}\right) d\bar{y} d\bar{x} \tag{21}$$

$$c_{55} = \frac{32(1 - \nu^2)}{\pi E_R R^3} \int_{-b^-}^{b^+} \int_0^a \bar{y} (1 - \bar{x}^2) F_{IX}^2\left(\frac{y}{h}\right) d\bar{y} d\bar{x} \tag{22}$$

where \bar{b}^- and \bar{b}^+ signify the normalized lower and upper bounds of the open region and x and y are local coordinates of the cracked region. An overbar signifies normalization by the shaft radius R . The shape functions F_{II} , F_{III} , F_{IX} , and F_{IV} are provided by Varney and Green [5]. The rotor material Poisson ratio is ν . The crack geometry, along with the CCL, is shown in Fig. 4. The CCL position is specified by the bounds b^- and b^+ , which are determined by evaluating the stress intensity function for the first mode of crack opening, K_I , at every point along the outer crack edge (modes II and III do not meaningfully contribute to crack breathing [13]). Here, only the rotor weight is assumed to contribute significantly to the crack breathing behavior (i.e., the rotor speed is beneath the first critical speed), though this assumption could be relaxed in future works at the expense of computational expediency. The stress intensity functions depend on the local axial stresses σ_1 at the crack, the shape functions used to calculate each compliance, and the crack geometry. The stresses, in turn, depend on the internal bending

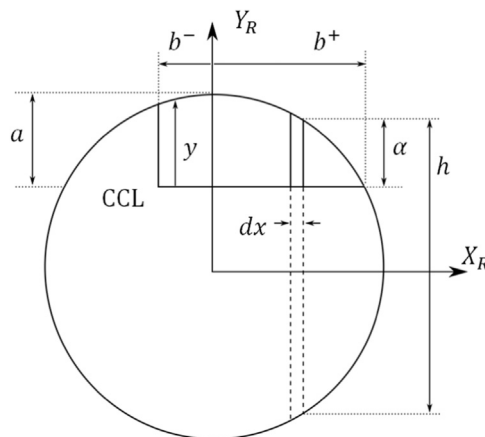


Fig. 4. Crack cross-section showing the CCL and the crack boundaries.

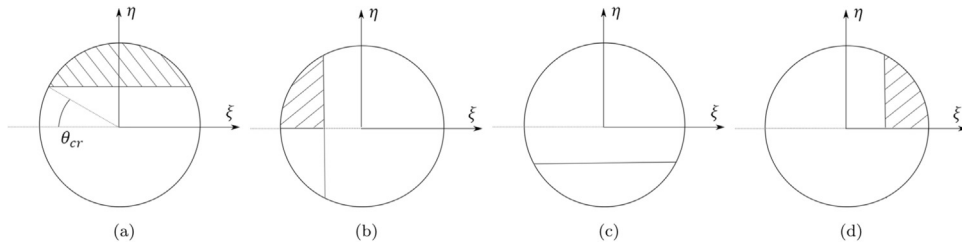


Fig. 5. Crack breathing behavior for various orientations, where gravity acts in the negative η direction. Shading indicates open regions of the crack; (a) $\alpha(t) = 0$, (b) $\alpha(t) = \pi/2$, (c) $\alpha(t) = \pi$, (d) $\alpha(t) = 3\pi/2$.

moments generated by the rotor weight. The total stress intensity function K_I at location x along the outer crack edge, where x is a local coordinate that extends along the crack edge, is found by summing the stress intensity functions caused by moments about X_R and Y_R :

$$K_I = K_{I, X_R} + K_{I, Y_R} \quad (23)$$

This approach is permissible because the stress intensity functions are scalar quantities. Using the expressions for stress provided by previous researchers [16,13] and evaluating the moments at the crack cross section caused by the rotor weight in the rotating frame gives the following forms for K_{I, X_R} and K_{I, Y_R} :

$$K_{I, X_R} = \frac{4(m_R g \cos \alpha) L_2 \sqrt{R^2 - x^2} \sqrt{\pi y} F_{IX}(y/h)}{\pi R^4} \quad (24)$$

$$K_{I, Y_R} = - \frac{4(m_R g \sin \alpha) L_2 x \sqrt{\pi y} F_{IY}(y/h)}{\pi R^4} \quad (25)$$

The location where K_I changes from negative to positive denotes the location where the crack cross-section changes from closed to open. This location is a function of angular position $\alpha(t)$ because gravity is a rotating force in the rotor-fixed $X_R Y_R Z_R$ frame. The region over which the crack remains fully-open or fully-closed is defined by the angle θ_{cr} :

$$\theta_{cr} = \tan^{-1} \left(\frac{R - a}{b} \right) \quad (26)$$

where b is the half-width of the fully-open crack (see Fig. 2). Thus, the crack remains fully-open for $-\theta_{cr} < \alpha(t) < \theta_{cr}$ and fully-closed for $\pi - \theta_{cr} < \alpha(t) < \pi + \theta_{cr}$.

Evaluating the crack compliance integrals is computationally expensive when performing the rotor stability analysis (or solving the rotor equations of motion). Because the compliances vary periodically, they can be expressed as a sum of complex exponentials with fundamental period $2\pi/\omega_r$. Recognizing this, the fast Fourier transform is calculated for each compliance

$$c_{ij}(t) \xrightarrow{\mathcal{F}} C_{ij}(\omega) \quad (27)$$

and then used to create an expedient reconstruction expression:

$$c_{ij}^* = \Re \left\{ \frac{1}{2} C_{ij}^0 + \sum_{k=1}^N |C_{ij}^k| \exp[i(k\omega_r t + \phi^k)] \right\} \quad (28)$$

where $\Re(\bullet)$ denotes the real part of the expression, C_{ij}^0 is the mean value over one period, N is the desired number of harmonics, $|C_{ij}^k|$ is the modulus of $C_{ij}(\omega)$ evaluated at the k th harmonic, and ϕ^k is the phase of $C_{ij}(\omega)$ at the k th harmonic. This expression is analytic with respect to time, and only relies on the crack compliances calculated over a single revolution. The compliances are calculated over one period for a crack depth of 40%, and shown along with their Fourier reconstruction in Fig. 6 (note the similarity between these results and those presented by Chasalevris and Papadopoulos [12] for another breathing function). Here, each compliance is sufficiently reconstructed from the Fourier transform using $N = 25$ harmonics. Importantly, the compliance calculations validate the angular bound θ_{cr} .

The compliance matrix of the cracked overhung shaft (Eq. 10) using the new time-dependent compliances is then inverted into the stiffness matrix and transformed from the shaft-fixed reference into the inertial $\xi\eta\zeta$ frame (see Eq. 17).

4. Floquet stability analysis

Floquet stability analysis is a powerful tool for determining the stability of dynamic systems with linear time-periodic coefficients. The objective here is to provide a practical method for performing Floquet stability analysis numerically; a

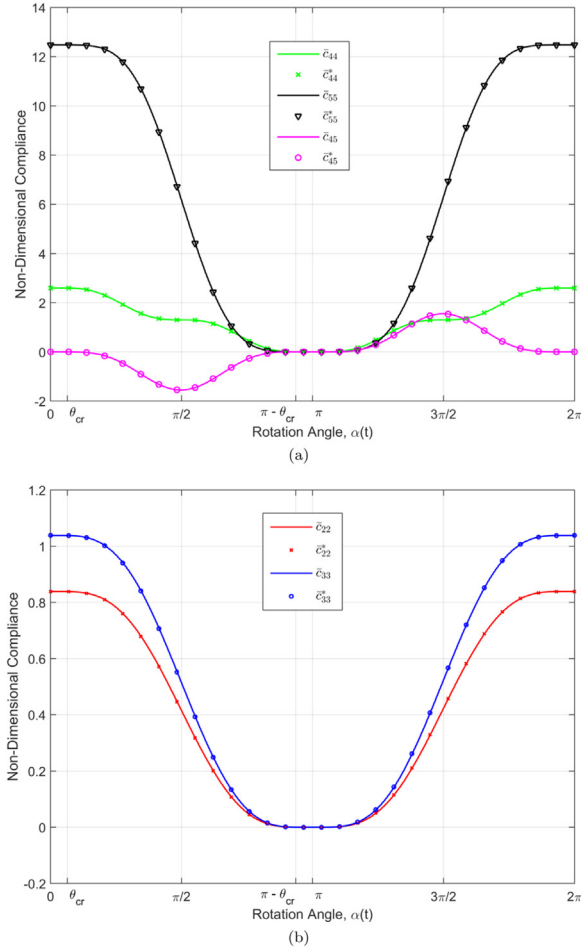


Fig. 6. CCL Breathing Crack: Non-dimensional crack compliances versus shaft rotation, showing a comparison between direct calculation and a Fourier transform approximation ($a/d = 40\%$, $E_R = 210$ GPa, $\nu = 0.3$, $d = 35$ mm, $L = 250$ mm, $L_1 = 0.05 L$); (a) angular crack compliances, (b) eccentric crack compliances.

thorough mathematical treatment of Floquet theory is provided elsewhere [24,25]. The premise of Floquet theory is that a first-order system of linear time-periodic (LTP) differential equations with fundamental period T can be rewritten such that

$$\mathbf{X}(t + T) = \Phi\mathbf{X}(t) \tag{29}$$

where the matrix Φ is called the monodromy matrix, and represents a Poincaré map that updates the vector solution \mathbf{X} at time t to the solution at time $t + T$. The objective is to determine if this mapping indicates convergence or divergence of the solution following a perturbation from the steady-state limit cycle. In general, however, the matrix Φ is not directly (i.e., analytically) obtainable. To obtain Φ , assume that a periodic solution vector $\mathbf{q}_0(t)$ exists with fundamental period T , and then introduce a perturbation $\Delta\mathbf{q}$:

$$\mathbf{q}(t) = \mathbf{q}_0(t) + \Delta\mathbf{q}(t) \tag{30}$$

Inserting this disturbance and its derivatives into Eq. (2) results in the autonomous perturbation equations for the overhung rotor:

$$\mathbf{M}_R\Delta\ddot{\mathbf{q}}_R + (\mathbf{D}_R + \mathbf{D}_V + \mathbf{G}_R)\Delta\dot{\mathbf{q}}_R + (\mathbf{K}(t) + \mathbf{D}_R^*)\Delta\mathbf{q}_R = \mathbf{0} \tag{31}$$

where matrix notation has been dropped for brevity. In first-order state space, the perturbation equations of motion are:

$$\dot{\mathbf{x}} = \mathbf{A}(t)\mathbf{x} \tag{32}$$

where the state vector is

$$\mathbf{x} = [\Delta\mathbf{q} \quad \Delta\dot{\mathbf{q}}]^T \tag{33}$$

The perturbation state space equations are now used to find the monodromy matrix Φ . The fundamental period T is divided into N intervals with length Δt , such that $T = N\Delta t$. Thus, if the number of intervals is large, the state matrix $\mathbf{A}(t)$ can be assumed constant over Δt , which then allows the equations to be integrated numerically over each finite interval. The initial conditions are assumed to be unity without loss of generality [24]. The numeric integration transfers the state vector at time t_i to the state vector at time $t_{i+1} = t_i + \Delta t$:

$$\mathbf{x}(t_{i+1}) = \mathbf{T}_i \mathbf{x}(t_i) \quad (34)$$

Thus, the monodromy matrix is the successive product of all the interval transfer matrices:

$$\Phi = \mathbf{T}_N \cdots \mathbf{T}_{i+1} \mathbf{T}_i \mathbf{T}_{i-1} \cdots \mathbf{T}_1 \mathbf{T}_0 \quad (35)$$

Here, the specific form of the transfer matrix \mathbf{T}_i is found by integrating the state-space equations of motion using the Newmark-Beta method, according to the procedure established by Guilhen et al. [26]:

$$\mathbf{T}_i = \begin{bmatrix} \mathbf{B}_0 & \mathbf{B}_1 \\ 2(\mathbf{B}_0 - \mathbf{I})/\Delta t & 2\mathbf{B}_1/\Delta t - \mathbf{I} \end{bmatrix} \quad (36)$$

where \mathbf{I} is the identity matrix and

$$\begin{aligned} \mathbf{B}_0 &= 4\mathbf{D}_0^{-1} \mathbf{M}_R / \Delta t \\ \mathbf{B}_1 &= \mathbf{D}_0^{-1} (4\mathbf{M}_R / \Delta t^2 + 2\mathbf{C} / \Delta t - \mathbf{E}_i) \\ \mathbf{D}_0 &= 4\mathbf{M}_R / \Delta t^2 + 2\mathbf{C} / \Delta t + \mathbf{E}_{i+1} \end{aligned} \quad (37)$$

where

$$\mathbf{E}_i = \mathbf{K}_i + \mathbf{D}_R^* \quad (38)$$

$$\mathbf{C} = \mathbf{D}_R + \mathbf{D}_v + \mathbf{G}_R \quad (39)$$

These matrices can be modified if the damping matrix is also linear time-periodic (such a condition is not encountered in this work). Stability is then determined by finding the eigenvalues of Φ , which in this context are the Floquet multipliers λ_f :

$$|\Phi - \lambda_f \mathbf{I}| = 0 \quad (40)$$

These multipliers determine the local orbital convergence or divergence of the solution following one iteration of the minimal period T . The solution $\mathbf{x}(t)$ is asymptotically stable if the modulus of every λ_f is less than unity, which guarantees the existence of a stable limit cycle (i.e., periodic attractor) (a Floquet multiplier of unity does not guarantee asymptotic stability). That is, any perturbation from the limit cycle results in the solution returning to the limit cycle. On the other hand, the solution is divergent (i.e., unstable) if the modulus of any Floquet multiplier is greater than unity.

5. Results

The Floquet stability analysis is performed separately for an open crack and a breathing crack, where the parameters for the rotor are given in Table 1. An experimental method for determining the internal damping coefficient β_c is presented by Casey and Green [3], who provide an estimate of $\beta_c = 0.01$. In all cases considered here, the crack is located a distance $L_1 = 0.05L$ from the support. In the results, a thin rotor refers to the case where $I_{pR} = 2I_{tR}$, while the thick rotor designation refers to the case where $I_{pR} = 0.5I_{tR}$. Furthermore, the matrix Φ is generated numerically using 150 time steps per period.

Table 1
Overhung rotor parameters.

Parameter	
Rotor mass, m_R	20 kg
Rotor transverse mass moment of inertia, I_{tR}	0.2 kg · m ²
Rotor polar mass moment of inertia, I_{pR}	(variable)
Shaft diameter, d	35 mm
Shaft length, L	250 mm
Shaft elastic modulus, E_R	210 GPa
Proportional damping coefficient, β_c	0.01

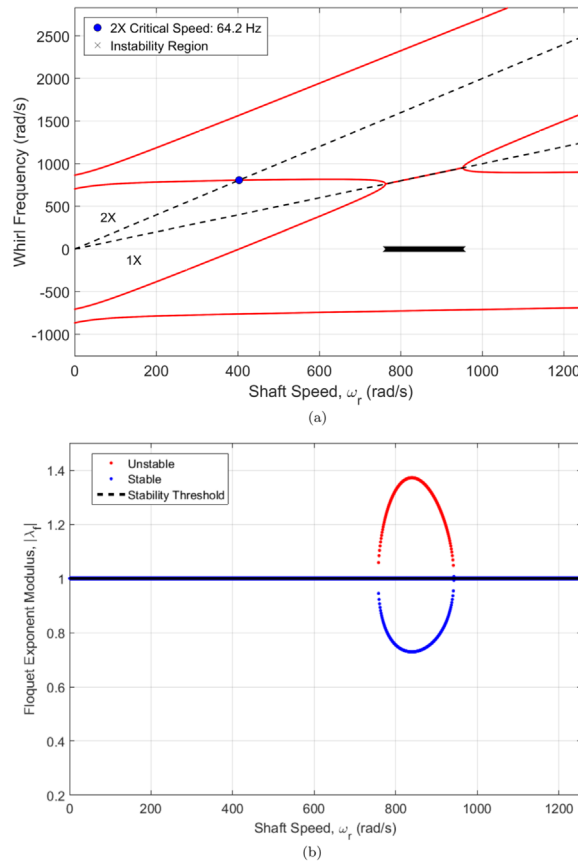


Fig. 7. Validating the rotor stability analysis for an undamped rotor (i.e., $\beta_c = \zeta_c = \zeta_r = 0$); (a) stability calculated using a conventional eigenvalue analysis, (b) stability calculated using Floquet stability analysis.

5.1. Open crack stability

The rotor stability considering an open crack can be calculated in the rotating frame using a conventional eigenvalue analysis [3] or in the inertial frame using Floquet stability analysis. In this work, the stability analysis of the rotor with an open crack is performed using Floquet stability analysis. This choice is made to facilitate comparison with the rotor breathing crack stability results, which cannot easily be analyzed using a routine eigenvalue analysis.

The Floquet stability analysis method is first verified by comparing the resulting instability bounds to those provided by Casey and Green [3], where instability was determined using a classical eigenvalue analysis in the rotating frame. For comparison with the results given therein, the analysis is performed for the undamped overhung rotor using the test rig parameters provided by Casey [37]. The resulting Campbell diagram (i.e., the locus of eigenvalues versus shaft speed) is shown in Fig 7a for an open crack of depth 40%. In the classical eigenvalue analysis, the instability region is identified by an eigenvalue with a positive real component (i.e., $\omega_r = 758 \text{ rad/s} - 942 \text{ rad/s}$). The Floquet stability analysis gives lower and upper instability bounds of 763 rad/s and 952 rad/s, respectively. These estimates are sufficiently close considering that the Floquet stability method is predicated on solving the equations of motion numerically using the Newmark-Beta method.

The stability analysis is now performed for the parameters specified in Table 1. The Floquet exponents λ_f are obtained across a range of shaft speeds for an open crack whose depth is 40% of the shaft diameter, and the moduli $|\lambda_f|$ are shown in Figs. 8 and 9 for a thin and thick rotor, respectively. For each case, two scenarios are investigated: no external viscous damping ($\zeta_c = \zeta_r = 0$) and small external viscous damping ($\zeta_c = \zeta_r = 0.01$). In both cases, an external viscous damping ratio of 1% prominently reduces the extent of rotor instability versus both shaft speed and crack depth. Without external viscous damping, the rotor response remains unstable with increasing shaft speed once the first local region of instability is encountered. This broad range of instability is a consequence of internal damping β_c , and occurs in a similar fashion even when $a = 0\%$. In general, the gyroscopic effect stabilizes the thin rotor over a wider range of shaft speeds than the thick rotor. Additionally, the thin rotor response over the considered shaft speed range shows only a single region of instability, whereas the thick rotor displays recurring regions of local instability.

The cracked rotor equations of motion are solved numerically to validate the stability predictions. Specifically, the validation is performed for the thick rotor with 1% external viscous damping and an open crack of 40% depth. The normalized

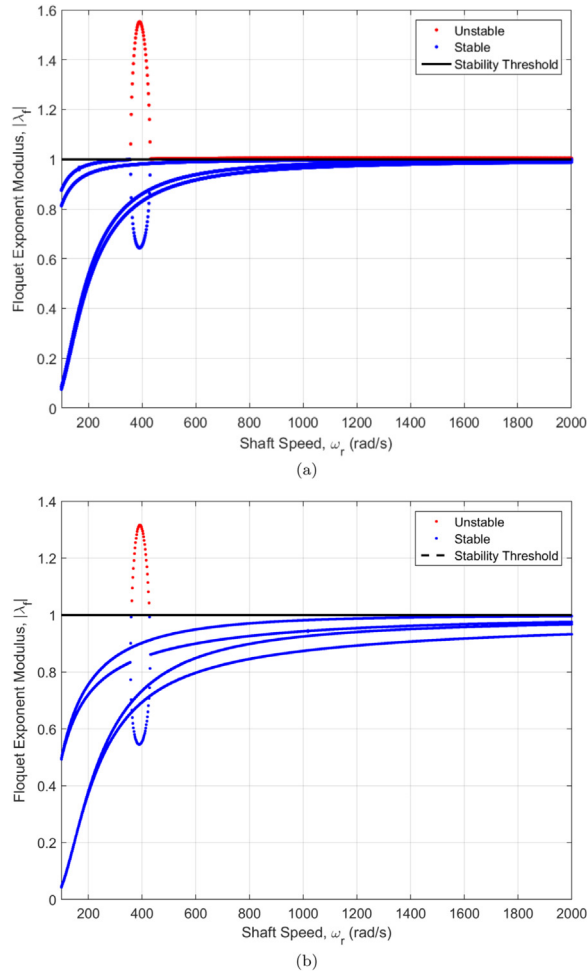


Fig. 8. Stability of a thin rotor with a 40% depth open crack ($I_{pR} = 0.4 \text{ kg} \cdot \text{m}^2$); (a) $\zeta_e = \zeta_\gamma = 0$, (b) $\zeta_e = \zeta_\gamma = 0.01$.

rotor eccentric response is shown in Fig. 10 for both a stable ($\omega_r = 280 \text{ rad/s}$) and unstable ($\omega_r = 320 \text{ rad/s}$) shaft speed near the first region of instability. The calculated responses are commensurate with the stability predictions gleaned from the Floquet stability analysis.

The existence of crack-induced instability was also observed experimentally in an overhung rotordynamic test rig (a description of the apparatus is provided by Varney and Green [5]). The test rig employs an overhung rotor with a finite-width notch created via electrical discharge machining. While modernizing the rotor test rig and associated data acquisition system, an undergraduate researcher unaware of crack-induced rotor instability operated the rotor at a speed within the instability region. The resulting rotor quickly experienced catastrophic failure, and is shown in Fig. 11. The original notch of depth 40% is shown in the figure, along with the crack which propagated due to operation within the instability region. The specific shaft speed at which the failure occurred is unknown due to the circumstances of the failure. This experience underscores the need to precisely predict the onset of crack-induced rotor instability.

The stability analysis is repeated over a wide range of crack depths and shown in Figs. 12–15 for external viscous damping ratios of 0%, 0.5%, 1%, and 2%, respectively (in the figures, the dark regions represent regions of instability). As observed previously, internal damping in the absence of external viscous damping results in an expansive region of rotor instability (see Fig. 12). This wide range of instability disappears when external viscous damping is included, as shown in Fig. 13. The figures indicate that once again, the thin rotor exhibits reduced instability regions compared to the thick rotor. For all cases presented here with external viscous damping, the thin rotor has only a single region of instability, whereas the thick rotor has multiple recurring instability regions. These instability regions are influenced by crack depth, a conclusion that has also been reached by previous researchers [3,8]. In all cases considered here, the shaft speed range over which the rotor response is unstable increases with increasing crack depth. If a crack is suspected, operating in (or even near, due to crack propagation) these instability regions can quickly result in catastrophic machine failure. This observation underscores the need to detect and rectify incipient rotor cracks.

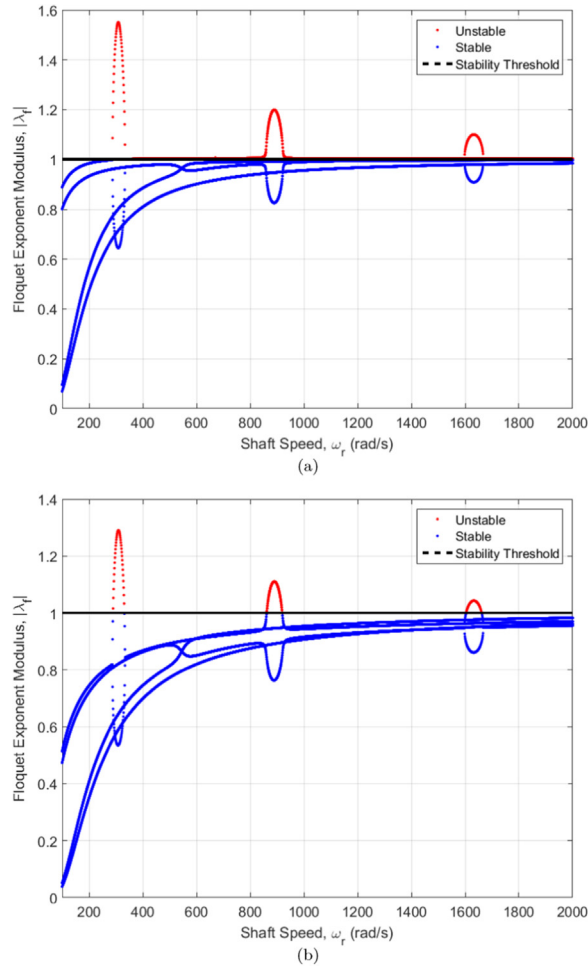


Fig. 9. Stability of a thick rotor with a 40% depth open crack ($I_{PR} = 0.1 \text{ kg} \cdot \text{m}^2$); (a) $\zeta_\epsilon = \zeta_\gamma = 0$, (b) $\zeta_\epsilon = \zeta_\gamma = 0.01$.

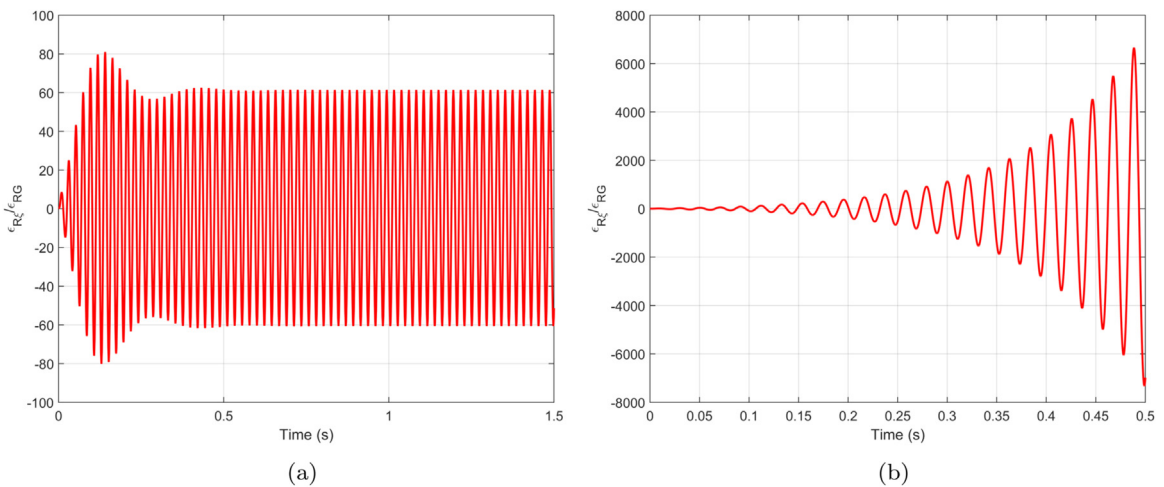


Fig. 10. Waveforms demonstrating selected unstable and stable shaft speeds, as predicted by Floquet stability analysis for the thick rotor with an open crack ($\zeta_\epsilon = \zeta_\gamma = 0.01$, $a = 40\%$) where $\epsilon_{RG} = 5 \text{ }\mu\text{m}$ and $\chi_R = 1 \text{ mrad}$; (a) stable: $\omega_r = 280 \text{ rad/s}$, (b) Unstable: $\omega_r = 320 \text{ rad/s}$.

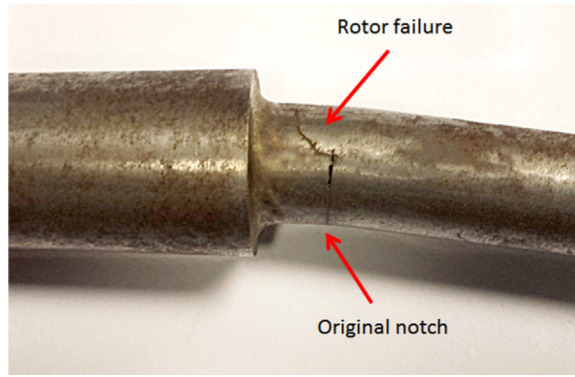


Fig. 11. Overhung rotor failure due to instability caused by an open crack.

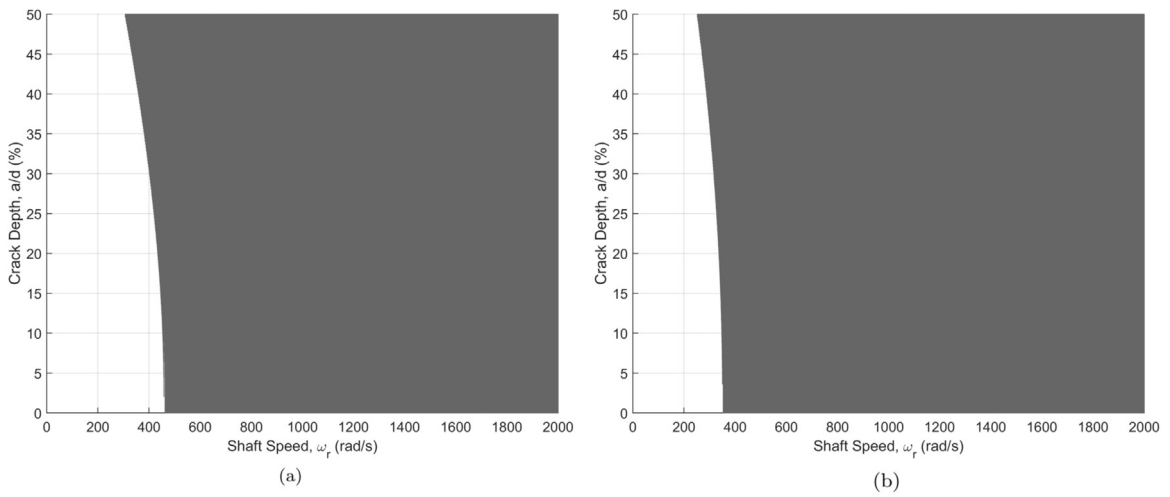


Fig. 12. Open Crack: Floquet stability with no external viscous damping ($\zeta_c = \zeta_\gamma = 0$); (a) thin rotor ($I_{pR} = 0.4 \text{ kg} \cdot \text{m}^2$), (b) thick rotor ($I_{pR} = 0.1 \text{ kg} \cdot \text{m}^2$).

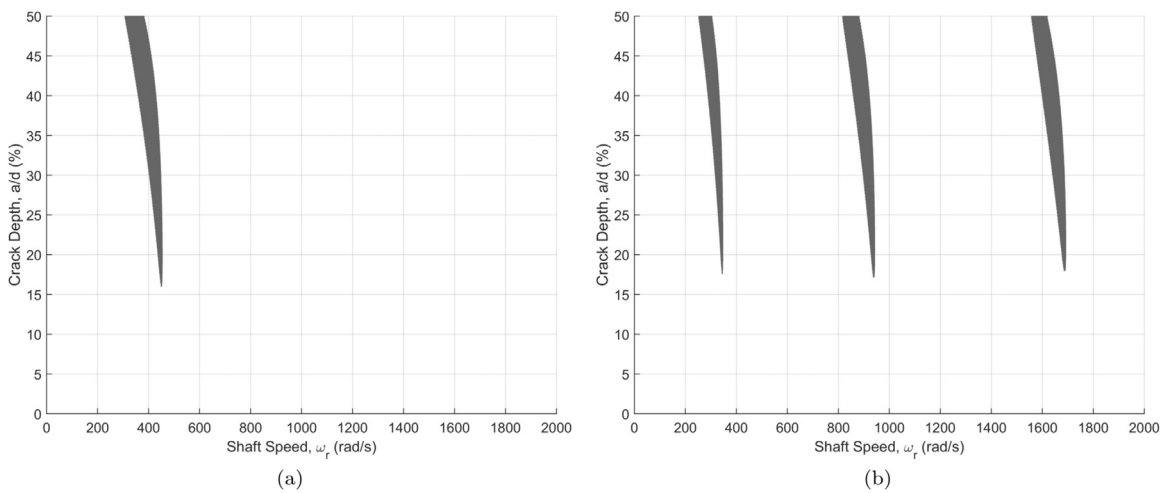


Fig. 13. Open Crack: Floquet stability with no external viscous damping ($\zeta_c = \zeta_\gamma = 0.005$); (a) thin rotor ($I_{pR} = 0.4 \text{ kg} \cdot \text{m}^2$), (b) thick rotor ($I_{pR} = 0.1 \text{ kg} \cdot \text{m}^2$).

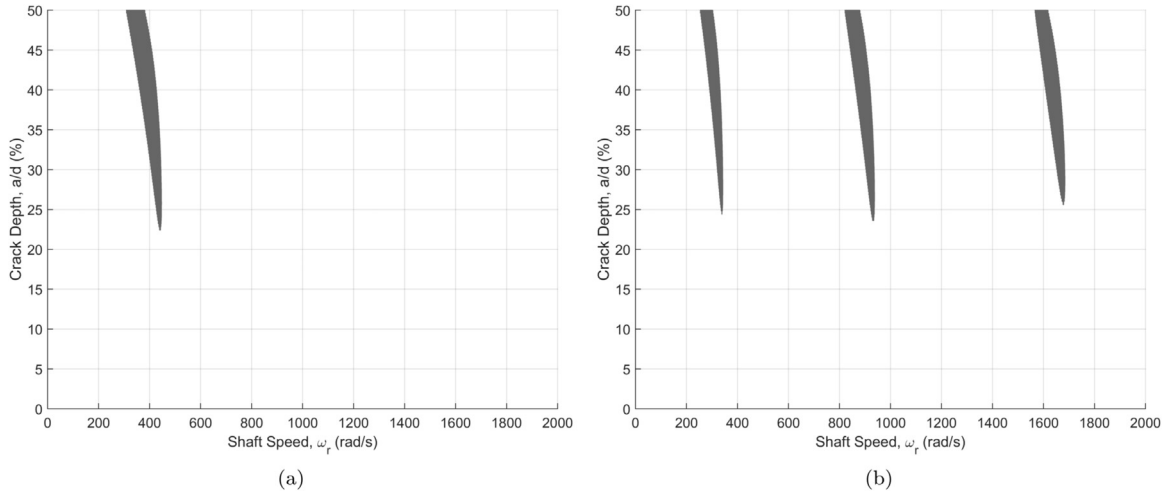


Fig. 14. Open Crack: Floquet stability with small external viscous damping ($\zeta_c = \zeta_\gamma = 0.01$); (a) thin rotor ($I_{PR} = 0.4 \text{ kg} \cdot \text{m}^2$), (b) thick rotor ($I_{PR} = 0.1 \text{ kg} \cdot \text{m}^2$).

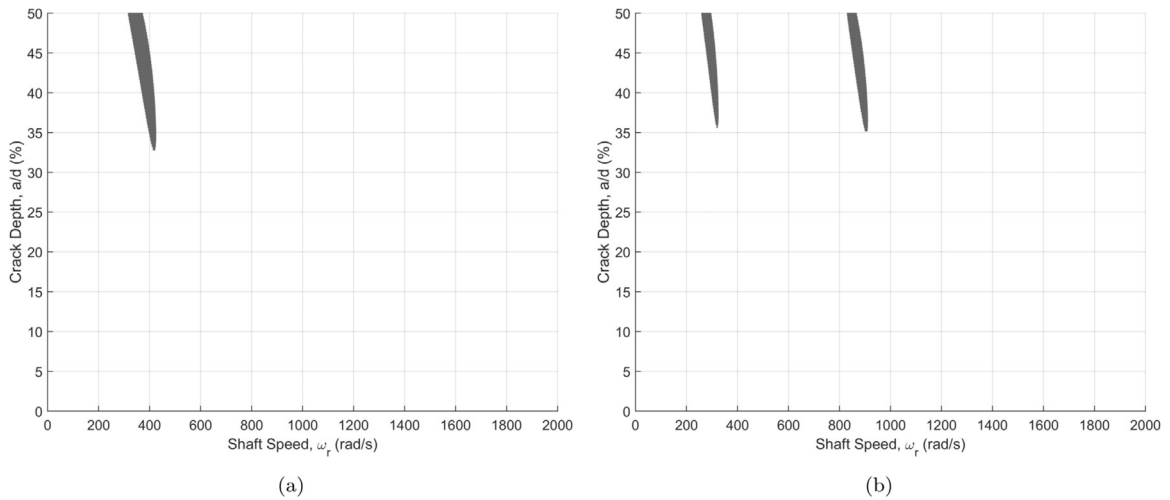


Fig. 15. Open Crack: Floquet stability with small external viscous damping ($\zeta_c = \zeta_\gamma = 0.02$); (a) thin rotor ($I_{PR} = 0.4 \text{ kg} \cdot \text{m}^2$), (b) thick rotor ($I_{PR} = 0.1 \text{ kg} \cdot \text{m}^2$).

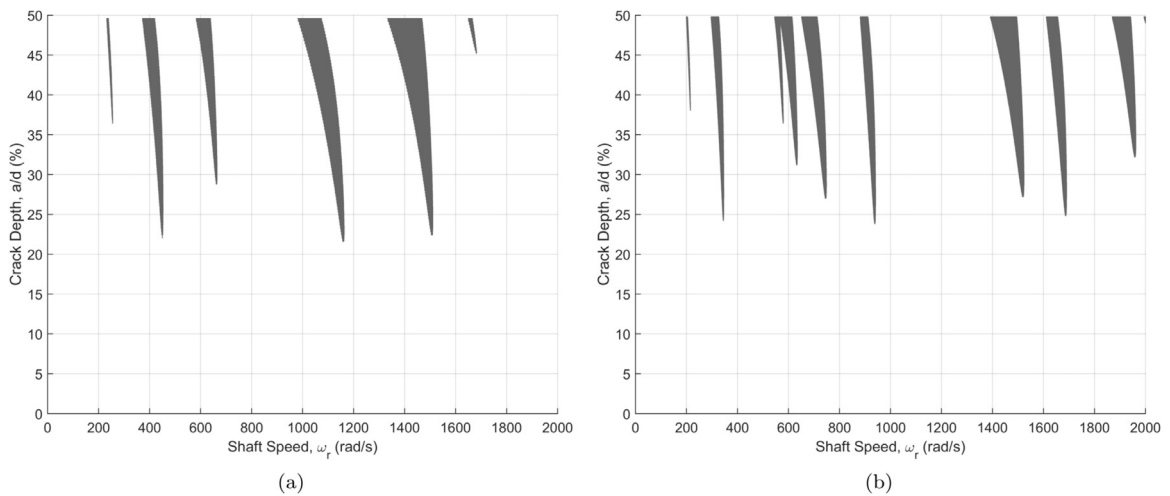


Fig. 16. Breathing Crack: Floquet stability ($\zeta_c = \zeta_\gamma = 0.005$); (a) thin rotor ($I_{PR} = 0.4 \text{ kg} \cdot \text{m}^2$), (b) thick rotor ($I_{PR} = 0.1 \text{ kg} \cdot \text{m}^2$). The forward critical speed for the thin rotor is approximately 465 rad/s, while the forward critical speeds for the thick rotor are 353 rad/s and 1714 rad/s.

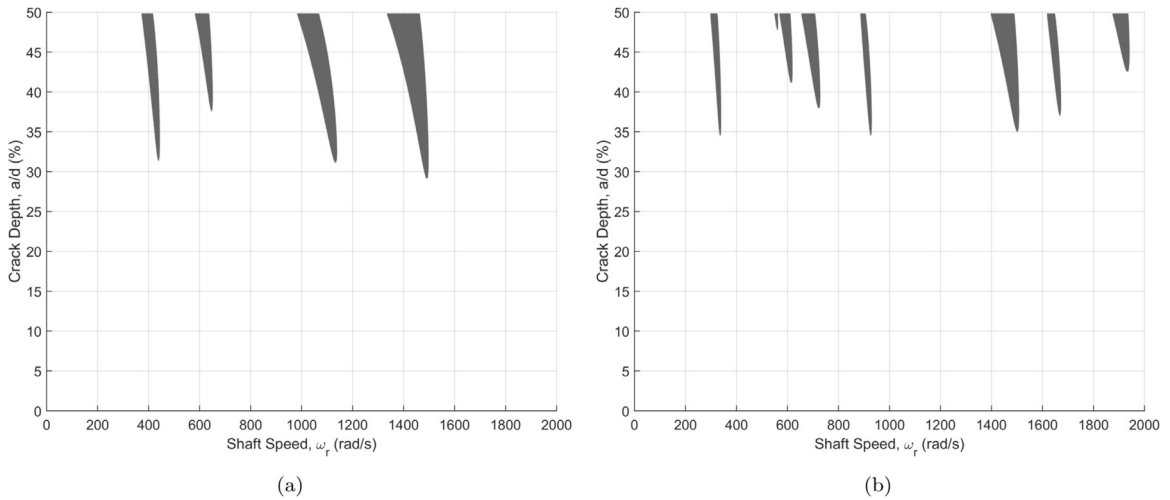


Fig. 17. Breathing Crack: Floquet stability ($\zeta_e = \zeta_\gamma = 0.01$); (a) thin rotor ($I_{pR} = 0.4 \text{ kg} \cdot \text{m}^2$), (b) thick rotor ($I_{pR} = 0.1 \text{ kg} \cdot \text{m}^2$).

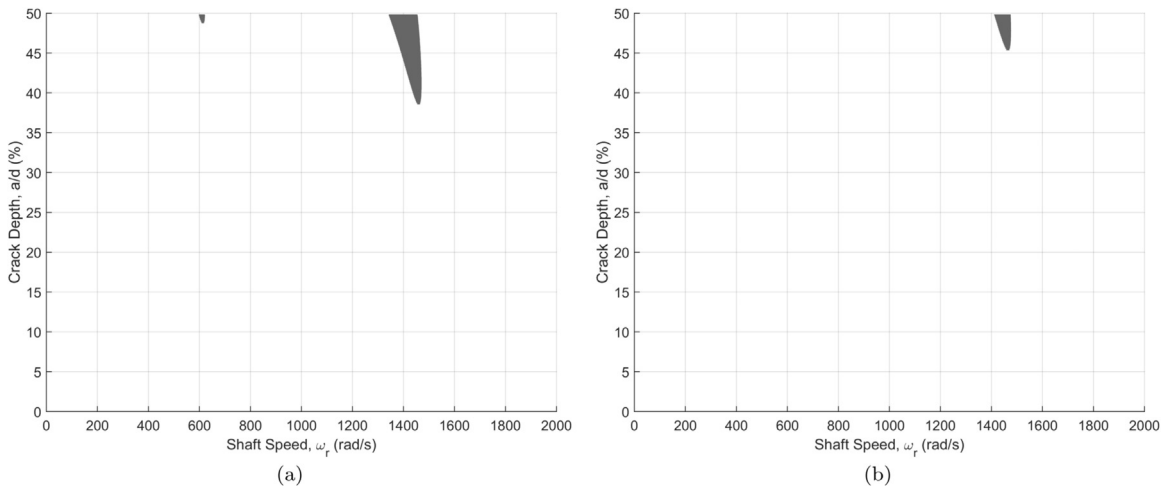


Fig. 18. Breathing Crack: Floquet stability ($\zeta_e = \zeta_\gamma = 0.02$); (a) thin rotor ($I_{pR} = 0.4 \text{ kg} \cdot \text{m}^2$), (b) thick rotor ($I_{pR} = 0.1 \text{ kg} \cdot \text{m}^2$).

5.2. Breathing crack stability

The rotor stability considering a breathing crack is calculated using Floquet stability analysis and shown in Figs. 16–18 for external viscous damping ratios of 0.5%, 1%, and 2%, respectively. Similar to the open crack, the rotor stability once again depends strongly on the external damping ratio, the rotor thickness, and the crack depth. Several important conclusions are drawn from the analysis, and are generally similar to those gleaned from the open crack analysis:

1. The rotor instability shaft speed range increases with increasing crack depth.
2. Increasing the external viscous damping ratio decreases the extent and prevalence of localized crack-induced instability regions.
3. The breathing crack generates more localized instability regions for a thick rotor than a thin rotor, except for the case of high external viscous damping.

Still, there are several important differences between the rotor stability with an open versus breathing fatigue crack. These differences are most prominently observed regarding the prevalence of instability regions (i.e., the number of branches on the instability plots) and the approximate lower threshold of crack depth abetting instability (i.e., the shallowest crack over the considered shaft speed range that causes instability):

1. For small external viscous damping ratios, the breathing crack causes more regions of rotor instability than the commensurate open crack.
2. For a given external damping ratio, the open crack model predicts instability for shallower cracks than the breathing model predicts. For example, comparing Figs. 13b and 16b, the lower threshold of crack depth causing instability is approximately 17% for the open crack and 24% for the breathing crack. This observation is valid for both thin and thick rotors.

It is also interesting to note that the thick rotor has more branches of instability than the thin rotor because the thick rotor has an additional forward critical speed, and thus, a greater propensity for parametric resonance. Furthermore, as the crack increases in depth, the forward critical speed(s) decrease in frequency; this decrease is likewise observed in the instability region branches. Accurately predicting rotor instability therefore hinges on accurately identifying an appropriate crack model. To reiterate, the stability predictions are important because they provide an upper limit on crack depth beyond which catastrophic failure occurs via the onset of instability. The crack must be detected before its propagation causes rotor failure.

6. Conclusions

This work has presented a numeric Floquet stability analysis for a cracked overhung rotor with linear time-periodic stiffness coefficients. The rotor model is presented in the inertial reference frame, and includes gyroscopic effects, external viscous damping, and internal structural damping. Two different types of cracks were considered here: an open crack and a breathing fatigue crack. In both cases, the crack compliance is calculated using the strain energy release rate. The breathing crack compliances are evaluated versus rotor rotation using the crack closure line method, and subsequently approximated using the Fourier transform (this provides an expedient method for evaluating the breathing crack stiffness during the numeric stability analysis). The global rotor stiffness matrix is then obtained in closed-form using transfer matrix methods, resulting in a time-dependent stiffness matrix (and specifically, linear time-periodic coefficients).

The stability analysis is then performed over a range of crack depths for different values of external viscous damping and rotor inertia. In all cases, and for both cracks, several key conclusions are observed. First, the range of shaft speeds over which the rotor is unstable increases with increasing crack depth. Second, the range of instability is dramatically reduced by even small increases in external viscous damping. Finally, it is observed for both crack types that the thick rotor displays more local regions of instability than the commensurate thin rotor. Several differences are also observed when comparing the stability of the rotor with the open crack and the breathing crack. In general, the breathing crack induces more localized regions of instability than the open crack. However, instability occurs at shallower crack depths when the crack is open than when it is breathing. These conclusions underscore the importance of accurately modeling the rotor, the damping conditions, and the specific crack behavior.

References

- [1] D. Bently, A. Muszynska, Early detection of shaft cracks on fluid-handling machines, in: Proceedings of ASME International Symposium on Fluid Machinery Trouble Shooting, 7, Anaheim, CA, pp. 287–296.
- [2] G. Sabnavis, R.G. Kirk, M. Kasarda, D. Quinn, Cracked shaft detection and diagnostics: a literature review, *Shock Vib. Dig.* 36 (2004) 287–296.
- [3] I. Green, C. Casey, Crack detection in a rotor dynamic system by vibration monitoring - part i: analysis, *J. Eng. Gas Turbines Power* 127 (2005) 425–436.
- [4] A.D. Dimarogonas, S. Paipetis, *Analytical Methods in Rotor Dynamics*, Applied Science Publishers, 1983.
- [5] P. Varney, I. Green, Crack detection in a rotordynamic system by vibration monitoring - part ii: extended analysis and experimental results, *J. Eng. Gas Turbines Power* 134 (2012) 112501.1–112501.10.
- [6] P. Varney, I. Green, Rotordynamic crack diagnosis: distinguishing crack location and depth, *J. Eng. Gas Turbines Power* 135 (2013) 112101.1–112101.8.
- [7] C.A. Papadopoulos, The strain energy release rate approach for modeling cracks in rotors: a state-of-the-art review, *Mech. Syst. Signal Process.* 22 (2008) 763–789.
- [8] R. Gasch, Dynamic behavior of the laval rotor with a transverse crack, *Mech. Syst. Signal Process.* 22 (2008) 790–804.
- [9] I. Mayes, W.G.R. Davies, Analysis of the response of a multi-rotor-bearing system containing a transverse crack in a rotor, *J. Vib. Acoust. Stress Reliab.* 106 (1984) 139–145.
- [10] C. Guo, M.A. Al-Shudeifat, J. Yan, L.A. Bergman, D.M. McFarland, E.A. Butcher, Application of empirical mode decomposition to a jeffcott rotor with a breathing crack, *J. Sound Vib.* 332 (2013) 3881–3892.
- [11] K.S. Wang, D. Guo, P.S. Heyns, The application of order tracking for vibration analysis of a varying speed rotor with a propagating transverse crack, *Eng. Fail. Anal.* 21 (2012) 91–101.
- [12] A.C. Chasalevris, C.A. Papadopoulos, A continuous model approach for cross-coupled bending vibrations of a rotor-bearing system with transverse breathing crack, *Mech. Mach. Theory* 44 (2009) 1176–1191.
- [13] A. Darpe, K. Gupta, A. Chawla, Coupled bending, longitudinal, and torsional vibrations of a cracked rotor, *J. Sound Vib.* 269 (2004) 33–60.
- [14] A. Dimarogonas, C.A. Papadopoulos, Vibration of cracked shafts in bending, *J. Sound Vib.* 91 (1983) 583–593.
- [15] T.H. Patel, A.K. Darpe, Influence of crack breathing model on nonlinear dynamics of a cracked rotor, *J. Sound Vib.* 311 (2008) 953–972.
- [16] C.A. Papadopoulos, A.D. Dimarogonas, Coupled longitudinal and bending vibrations of a rotating shaft with an open crack, *J. Sound Vib.* 117 (1987) 81–93.
- [17] C.A. Papadopoulos, A.D. Dimarogonas, Coupled longitudinal and bending vibrations of a cracked shaft, *J. Vib. Acoust. Stress, Reliab. Des.* 110 (1988) 1–8.
- [18] A. Ebrahimi, M. Heydari, M. Behzad, A continuous vibration theory for rotors with an open edge crack, *J. Sound Vib.* 333 (2014) 3522–3535.
- [19] N. Bachschmid, E. Tanzi, Deflections and strains in cracked shafts due to rotating loads: a numerical and experimental analysis, *Int. J. Rotating Mach.* 9 (2003) 303–311.
- [20] J.L. Zapica-Valle, E. Rodriguez, M. Garcia-Dieguez, J. Cortizo, Rotor crack identification based on neural networks and modal data, *Meccanica* 49 (2014) 305–324.

- [21] A.K. Darpe, A novel way to detect transverse surface crack in a rotating shaft, *J. Sound Vib.* 305 (2007) 151–171.
- [22] J. Sinou, An experimental investigation of condition monitoring for notched rotors through transient signals and wavelet transform, *Exp. Mech.* 49 (2009) 683–695.
- [23] J.T. Sawicki, A.K. Sen, G. Litak, Multiresolution wavelet analysis of the dynamics of a cracked rotor, *Int. J. Rotating Mach.* (2009) 1–8.
- [24] H. Sandberg, E. Mollerstedt, B. Bernhardsson, Frequency-domain analysis of linear time-periodic systems, *IEEE Trans. Autom. Control* 50 (2005) 1971–1983.
- [25] A.H. Nayfeh, B. Balachandran, *Applied Nonlinear Dynamics: Analytical, Computational, and Experimental Methods*, Wiley-VCH, 2004.
- [26] P.M. Guilhen, P. Berthier, G. Ferraris, M. Lalanne, Instability and unbalance response of dissymmetric rotor-bearing systems, *J. Vib. Acoust.* 110 (1988) 288–294.
- [27] S. Huang, Y. Huang, S. Shieh, Vibration and stability of a rotating shaft containing a transverse crack, *J. Sound Vib.* 162 (1993) 387–401.
- [28] C. Guo, M.A. Al-Shudeifat, J. Yan, L.A. Bergman, D.M. McFarland, E.A. Butcher, Stability analysis for transverse breathing cracks in rotor systems, *Eur. J. Mech. A/ Solids* 42 (2013) 27–34.
- [29] A. Sekhar, J.K. Dey, Effects of cracks on rotor system instability, *Mech. Mach. Theory* 35 (2000) 1657–1674.
- [30] G. Meng, R. Gasch, Stability and stability degree of a cracked flexible rotor supported on journal bearings, *J. Vib. Acoust.* 116 (2000) 116–125.
- [31] Y. Fu, Y. Zheng, Z. Hou, Analysis of non-linear dynamic stability for a rotating shaft-disk with a transverse crack, *J. Sound Vib.* 257 (2002) 713–731.
- [32] J. Sinou, Effects of a crack on the stability of a non-linear rotor system, *Int. J. Non-Linear Mech.* 42 (2007) 959–972.
- [33] Y. Luo, Z. Ren, H. Ma, T. Yu, B. Wen, Stability of periodic motion on the rotor-bearing system with coupling faults of crack and rub-impact, *J. Mech. Sci. Technol.* 21 (2007) 860–864.
- [34] R. Ricci, P. Pennacchi, Discussion of the dynamic stability of a multi-degree-of-freedom rotor system affected by a transverse crack, *Mech. Mach. Theory* 58 (2012) 82–100.
- [35] G. Genta, *Dynamics of Rotating Systems*, Mechanical Engineering Series, Springer Science and Business Media, Inc., New York, NY, 2005.
- [36] P. Varney, *Transverse Fatigue Crack Diagnosis in a Rotordynamic System Using Vibration Monitoring*, Master's thesis, Georgia Institute of Technology, 2013.
- [37] C. Casey, *Crack Detection in a Rotordynamic System by Vibration Monitoring*, Master's thesis, Georgia Institute of Technology, 2000.